

# Deterministic World Models for Verification of Closed-loop Vision-based Systems

Yuang Geng<sup>1</sup>[0000–0002–2265–7586], Zhuoyang Zhou<sup>1</sup>[0009–0007–0239–4268],  
Zhongzheng Zhang<sup>1</sup>[0009–0009–3589–1791], Siyuan Pan<sup>1</sup>[0009–0000–5915–5400],  
Hoang-Dung Tran<sup>1</sup>[0000–0001–6946–9526], and Ivan  
Ruchkin<sup>1</sup>[0000–0003–3546–414X]

<sup>1</sup>University of Florida, Gainesville, FL, USA

{yuang.geng,zhou.zhuoyang,renzhongzh.zhang,pansiyuan,dungtran}@ufl.edu,  
iruchkin@ece.ufl.edu

**Abstract.** Verifying closed-loop vision-based control systems remains a fundamental challenge due to the high dimensionality of images and the difficulty of modeling visual environments. While generative models are increasingly used as camera surrogates in verification, their reliance on stochastic latent variables introduces unnecessary overapproximation error. To address this bottleneck, we propose a *Deterministic World Model (DWM)* that maps system states directly to generative images, effectively eliminating uninterpretable latent variables to ensure precise input bounds. The DWM is trained with a dual-objective loss function that combines pixel-level reconstruction accuracy with a control difference loss to maintain behavioral consistency with the real system. We integrate DWM into a verification pipeline utilizing Star-based reachability analysis (StarV) and employ conformal prediction to derive rigorous statistical bounds on the trajectory deviation between the world model and the actual vision-based system. Experiments on standard benchmarks show that our approach yields significantly tighter reachable sets and better verification performance than a latent-variable baseline.

**Keywords:** Reachability Verification · Convolutional Neural Networks · World Models · Conformal Prediction.

## 1 Introduction

Closed-loop vision-based control systems are increasingly used in safety-critical domains [9, 10, 38]. These systems rely on an end-to-end controller to process images and operate a physical plant [5, 19, 23]. The key advantage of end-to-end control is using the rich contextual and spatial information from raw images [15]. However, verifying the safety of such systems is hindered by two fundamental challenges: the difficulty of accurately modeling complex environments and the computational scalability bottleneck caused by high-dimensional images.

Symbolic techniques for verifiable modeling of visual environments rely on *rigid mathematical abstractions*, which fail to capture the complexity of real-world environments [20]. These methods derive a simplified symbolic representation of camera outputs based on geometric constraints [11, 25]. However, these

approaches are fundamentally limited to highly structured environments where the important elements of images are easy to describe symbolically, such as a lane-keeping car or an automated plane landing. Consequently, rigid symbolic models struggle to capture dynamic, unstructured environments where images vary significantly over time.

Instead, recent research has used *generative world models* as camera surrogates. In particular, conditional Generative Adversarial Networks (cGANs) [4] were trained to synthesize images conditioned on both the system state and stochastic latent variables [15]. These latent variables help with image reconstruction and cGAN training — but unfortunately introduce significant verification issues. Since latent variables *lack physical interpretability*, defining their valid input bounds for reachability analysis is inherently difficult. Meanwhile, widening the latent bounds can make reachable sets explode [3].

This paper proposes to verify vision-based systems with a **Deterministic World Model (DWM)** — a non-stochastic decoder that learns to map physical states to synthetic images. It represents a set of images that can be generated from a set of physical states, allowing seamless integration with reachability without abstraction or tedious manual modeling. The DWM is trained with a dual-objective loss: a typical image reconstruction loss ensures visual accuracy, and a *control difference loss* supports trajectories consistent with the real system.

Integrating DWM into the reachability analysis of vision-based systems faces a scalability challenge. DWM and the image-based controller are typically large convolutional neural networks. Their interaction with physical dynamics leads to rapidly growing overapproximation error over time. To mitigate this, we reduce the DWM’s input dimension to equal the state dimension and employ the Star/ImageStar reachset representation [29]. This approach is particularly efficient for propagating reachable sets through neural nets while maintaining tight guaranteed overapproximations, thereby overcoming the scalability challenge.

No matter how accurate a world model is, a critical question remains: what does the world model-based verification imply about the real system’s safety? *Conformal prediction (CP)* [26] is proposed to transfer the reachable set from the world model to the real system. To this end, we obtain a statistical bound on the *trajectory-based deviation* between two systems’ trajectories. Incorporating this bound into our verification yields tight guarantees for the real system.

We evaluated our approach on three standard control benchmarks: CartPole, MountainCar, and Pendulum. Our experiments show that our DWM approximates the real system better than the baselines do. This reduction in modeling uncertainty directly translates into superior verification performance, with high F1 scores and precise safety guarantees across all environments. In summary, the contributions of this paper are as follows:

1. A deterministic world modeling approach that creates verifiable generative surrogates of camera sensors.
2. The first adoption and extension of star-based reachability analysis for verification of closed-loop vision-based systems.
3. Extensive experiments on three OpenAI gym benchmarks showing superior verification accuracy compared to baselines.

## 2 Related Work

### 2.1 Open- and Closed-loop Verification

Neural network verification is primarily studied in two settings [16, 17]. *Open-loop verification* formally establishes the static input-output relationship of the network without dynamic feedback [30]. Recent research has made significant progress on open-loop verification of complex neural networks with techniques like abstract interpretation [22] and symbolic execution [33] and representations like zonotopes [16] and ImageStars [28, 32]. For instance, one can verify that a CNN correctly classifies a stop sign image subject to a 5% brightness distortion.

In contrast, *closed-loop verification* treats the network as a controller within a dynamical system, analyzing how its action influences future states [7, 14, 24]. Current tools such as NNV [18], POLAR [35], ReachNN [12] and Verisig [14] effectively verify controllers with low-dimensional state inputs. However, these methods cannot be directly applied to image-based controllers since the state-image mapping is analytically unavailable. Even if a mapping is established, propagating high-dimensional image sets through dynamics causes rapid error accumulation. To mitigate this, we strictly limit the mapping’s input dimensions to the physical state, avoiding the scalability bottlenecks inherent in image space.

### 2.2 Verification with Surrogate Sensor and Perception Models

Directly verifying end-to-end vision-based controllers is challenging because image inputs lack tractable physical semantics [21]. The core challenge lies in modeling how the physical state (e.g., position) translates into the next image observation [9]. One way to bridge this gap is with generative models, such as cGANs, as camera surrogates within the verification pipeline [3, 15]. These models map system states and stochastic latent variables to synthetic images.

However, our key insight is that *these latent dimensions detract from verification*. The original intent of stochastic latent variables is to capture diverse distributions with multiple modes and ensure smooth coverage of the latent space, rather than deterministically generate a specific image [36, 37]. For example, cGAN samples Gaussian latent variables to generate diverse variations of one image, a common data augmentation mechanism [13, 39]. Consequently, the latent space is intentionally optimized for variation, *not to produce accurate images*. This objective contradicts verification’s goal, which is to reason precisely about the images that arise from the true system’s states. Thus, we eliminate uninterpretable latent variables to make image generation precise and state-consistent.

### 2.3 Scalar Conformal Prediction

CP serves as a rigorous, distribution-free method for quantifying uncertainty by providing high-confidence error bounds [8, 26]. This method operates on a calibration dataset  $D = \{z_1, \dots, z_N\}$  of exchangeable scalar “non-conformity scores.” CP leverages the exchangeability property that the rank of a new, exchangeable test variable  $Z_{test}$  is uniformly distributed among the calibration samples [2]. Consequently, sorting these scores yields the  $(1 - \alpha)$  quantile,  $z_{(\lceil (N+1)(1-\alpha) \rceil)}$ ,

that serves as a statistically valid upper bound. This guarantees that any future non-conformity score, drawn from the same distribution, falls below this bound with a probability of at least  $1 - \alpha$  [1, 26]. Unlike our past work that bounds controller discrepancies [9] and perception errors [34], we will use conformal prediction to quantify the gap between the world model and the real system.

### 3 Background and Problem Setup

In this section, we formally model our closed-loop vision-based system, capturing the interaction between the physical plant dynamics and the vision-based neural controller. Finally, we offer two versions of our verification problem.

**Definition 1 (Closed-loop Vision-based System).** *A closed-loop vision-based system is defined as a tuple  $(S, O, U, P, C, f)$ , where  $S \subseteq \mathbb{R}^n$  is the state space,  $O \subseteq \mathbb{R}^{h \times w}$  is the image observation space, and  $U \subseteq \mathbb{R}^m$  is the control input space. At time step  $t$ , the camera sensor  $P : S \rightarrow O$  maps the true state  $s_t$  to an image  $o_t$ . The controller  $C : O \rightarrow U$  maps the image to a control action  $u_t$ . The next state  $s_{t+1}$  is obtained according to the dynamics  $f : S \times U \rightarrow S$ :*

$$s_{t+1} = f(s_t, C(P(s_t))). \quad (1)$$

Given the system in Definition 1, we assume access to a state-image paired dataset by uniformly sampling  $N$  states from the state space  $S$ . For each sampled state  $s$ , the corresponding image  $I = P(s)$  can be obtained from the camera, yielding the one-to-one dataset  $\mathcal{D}_{\text{train}} = \{(s_i, I_i)\}_{i=1}^N$ .

**Definition 2 (System Trajectory).** *From an initial state  $s_0 \in I$ , the system evolves through state  $s_t$  at step  $k$  recursively by applying control actions derived from images of previous states per Equation 1. After executing for  $T$  steps, this process results in a trajectory  $\tau(s_0, T) = [s_0, s_1, \dots, s_T]$ .*

Defining desirable trajectory properties, such as reaching the goal or avoiding unsafe states, directly on images is inherently intractable. Images lack explicit geometric semantics, making it difficult to formulate universal rules for what constitutes a “safe pixel” or a “goal set of pixels.” Instead, our specifications must happen in the physical state space  $S$ , where quantities such as position and velocity have precise geometric meaning and evolve within the system in Definition 1. Therefore, we focus on computing the reachable sets  $\mathcal{R}_t(S_0)$ .

**Definition 3 (Reachable Set and Tube).** *Given a set of initial states  $S_0$  in system from Definition 1, the reachable set  $\mathcal{R}_t$  contains all possible physical states at time step  $t$  starting from any  $s_0 \in S_0$ . Thus, the reachable set  $\mathcal{R}_t$  at step  $t$  is defined as:*

$$\mathcal{R}_t(S_0) = \{s_t \mid \forall s_0 \in S_0\}.$$

*The reachable tube over the time  $[0, t]$  is defined as  $\mathcal{R}_{[0, t]}(S_0) = \bigcup_{i=0}^t \mathcal{R}_i(S_0)$ .*

*Reachability Problem.* Given an initial state set  $S_0 \subset S$ , a goal set  $G \subset S$ , a time horizon  $T$ , and the vision-based system from Definition 1, our verification objective is to ensure that, starting from any state in  $S_0$ , the system always reaches the goal set  $G$  within  $T$  steps. Formally, we aim to verify that

$$\forall s_0 \in S_0 \cdot \mathcal{R}_T(S_0) \subseteq G \quad (2)$$

Unfortunately, performing reachability on the real vision-based system is computationally intractable: camera  $P$  lacks an analytical form. Instead, we substitute the camera with a verifiable, learning-based world model and compute reachability analysis on the surrogate system. However, this step introduces a modeling error. To account for it in practice, we relax our formulation to stochastic reachability given a dataset of real-world trajectories.

*Stochastic Reachability Problem.* Given the dataset  $\mathcal{D}$  of trajectories starting from initial states  $s_0$  sampled from some distribution  $D_0$ , the objective is to find a reachable tube  $\hat{\mathcal{R}}$  that contains a random system trajectory  $\tau(s_0 \sim D_0, T)$  with probability  $1 - \alpha$ :

$$\mathbb{P}_{s_0 \sim D_0} \left[ \forall t \in \{0, \dots, T\} : s_t \in \hat{\mathcal{R}}_t \right] \geq 1 - \alpha, \quad (3)$$

Suppose we solve this problem. Then, if our final reachable set is contained in the goal set  $G$ , the real system’s trajectory is also likely to reach the goal  $G$ :

$$\hat{\mathcal{R}}_T \subseteq G \implies \mathbb{P}_{s_0 \sim D_0} [s_T \in G] \geq 1 - \alpha. \quad (4)$$

To address the above problem, the rest of the paper takes two key steps:

- Section 4 designs a verifiable yet accurate generative model that can replace the camera for closed-loop reachability.
- Section 5 establishes a stochastic reachability guarantee on the actual vision-based system given a reachability guarantee on the surrogate system.

## 4 Deterministic World Modeling for Reachability

This section introduces our deterministic world model to bridge the gap between system dynamics and camera images, thereby enabling the verification of image-based controllers, as shown in Figure 1. During the verification phase, we partition the entire initial state space into smaller, uniform subsets to reduce unnecessary conservatism and allow for parallel verification. We then iterate through these subsets to calculate the reachable set for the system. This reachability analysis utilizes layer-wise approximation on both the state-based world model and the CNN controller.

Specifically, our approach consists of three main components: (i) constructing a paired image-state training dataset, (ii) training our state-based world model using a weighted combination of image reconstruction and controller difference losses, and (iii) performing Star-set-based reachability analysis through the trained world model and the image-based controller.

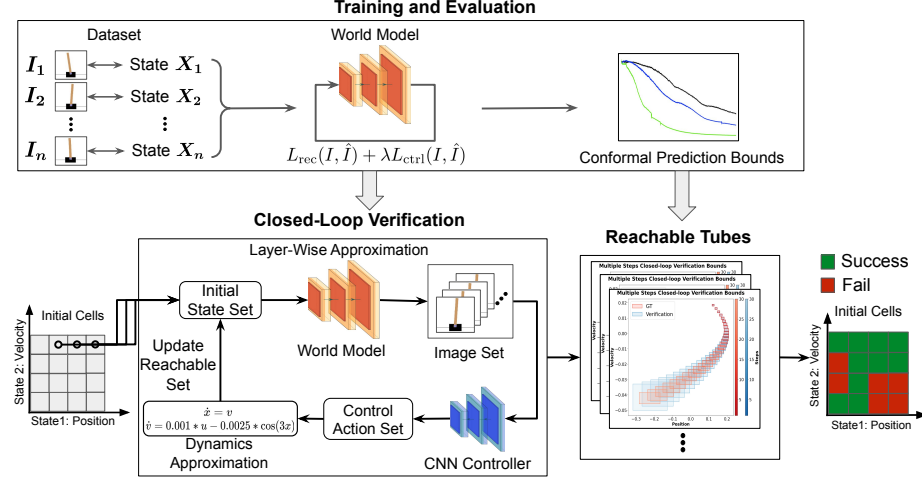


**Fig. 1.** Overview of our closed-loop verification framework. Our world model is first trained to generate images from states and evaluated with conformal prediction to bound trajectory mismatch. In closed-loop safety verification, we iterate over each initial set to calculate reachable sets with Star-based approximation.

*Training Dataset.* Our world model is trained to approximate the camera module  $P(s)$  using the dataset  $\mathcal{D}_{\text{train}} = \{(s_i, I_i)\}_{i=1}^N$ , mentioned in Section 3. Here, inputs are sampled uniformly from the state space and paired with ground-truth images to supervise the learning of the low-dimensional to high-dimensional mapping.

#### 4.1 Training Loss of Deterministic World Model

Our world model is implemented with a state-to-image decoder  $g_\theta : S \rightarrow \mathcal{I}$ , which takes a physical state  $s$  and outputs a reconstructed image  $\hat{I} = g_\theta(s)$ . The visual output has high dimensions  $H \times W$  (e.g.,  $96 \times 96$  grayscale). The architecture follows a typical design, with fully connected layers followed by transposed convolution (a.k.a. deconvolution) layers. It is trained with a weighted sum of two complementary losses: an image reconstruction loss and a controller difference loss.

*Image Reconstruction Loss.* This typical loss function enforces pixel-level fidelity between the true image  $I$  and the reconstructed image  $\hat{I}$ , with a modification to preserve semantically important regions. For instance, the vehicle and nearby objects are far more critical for control than the far-away background. To capture this distinction, we assign higher reconstruction weights to these priority areas and lower weights to the background. The weighted mean squared error (MSE) for the  $H \times W$  dimension image is defined below:

$$L_{\text{rec}}(I, \hat{I}) = \frac{1}{H \times W} \sum_{i=1}^H \sum_{j=1}^W w_{ij} (\hat{I}_{ij} - I_{ij})^2. \quad (5)$$

The weights  $w_{ij}$  are designed to emphasize important areas of the image, such as the object or track, based on pixel intensity:

$$w_{ij} = \begin{cases} w_h, & I_{ij} \leq \beta, \\ w_l, & I_{ij} > \beta, \end{cases} \quad (6)$$

where  $\beta$  represents a pixel intensity threshold. We discover that most objects of interest are darker than the background. Under a standard pixel definition, lower pixel values indicate darker regions (e.g.,  $I_{ij} \leq 20$  can represent dark gray). Therefore, the high weights  $w_h$  will be assigned to these dark regions, prioritizing over the brighter background. Our approach is extensible to more complex weight assignments depending on the case study.

*Controller Difference Loss.* The controller difference loss ensures that the reconstructed image produces a similar control behavior to the original image. This capability will help reduce the modeling error in Section 5.

Recall that per Definition 1,  $C(\cdot)$  is the image-based controller that maps an image to a control action  $u = C(I)$ . Inspired by a similar loss for image-based control repair [27], we penalize the discrepancy between the control actions derived from the reconstructed image and the original image:

$$L_{\text{ctrl}}(I, \hat{I}) = \|C(\hat{I}) - C(I)\|_2^2. \quad (7)$$

This loss,  $L_{\text{ctrl}}$ , ensures that our state-based world model preserves control-relevant features, rather than just reproducing visual similarities.

*Overall Objective.* The final loss combines the two above into a weighted sum:

$$L(\theta) = L_{\text{rec}}(I, \hat{I}) + \lambda L_{\text{ctrl}}(I, \hat{I}), \quad (8)$$

The  $\lambda$  balances the trade-off between visual accuracy and behavioral consistency. Minimizing  $L(\theta)$  over the dataset  $\mathcal{D}_{\text{train}}$  yields a model that is both visually accurate and controller-consistent.

## 4.2 Star-Set Approximation of the Trained World Model

To enable sound reachability analysis of the closed-loop system, we represent the uncertainty in the physical state using *Star sets* [29,31]. A Star set encodes all admissible states as an affine transformation of a low-dimensional predicate space:

$$S_0 = \{s = c_0 + V_0\alpha \mid C_0\alpha \leq d_0, \ell_0 \leq \alpha \leq u_0\}, \quad (9)$$

where  $c_0 \in \mathbb{R}^d$  is the center (the nominal state),  $V_0 \in \mathbb{R}^{d \times p}$  contains basis vectors describing the directions of uncertainty, and  $\alpha \in \mathbb{R}^p$  are predicate variables restricted by linear constraints  $C_0\alpha \leq d_0$  and element-wise bounds  $\ell_0 \leq \alpha \leq u_0$ .

This representation is convenient because any affine map  $s \mapsto As + b$  (e.g., fully connected and convolutional layers) allows for *exact* propagation of Star sets:

$$c' = Ac_0 + b, \quad V' = AV_0,$$

while nonlinear activation functions (e.g., ReLU, tanh, sigmoid) are propagated using the sound over-approximation techniques, which construct piecewise-linear upper and lower envelopes, from the StarV toolbox [29]. Full details of our verification procedure can be found in the appendix.

*Layer-wise Reachability.* A trained DWM  $g_\theta$  is a composition of  $n$  layers, denoted as  $g_\theta = L_n \circ \dots \circ L_1$ . To verify the output behavior, we perform layer-by-layer reachability analysis starting from the input Star set  $S_0$ , defined in Equation 9. Let  $R_{L_i}$  denote the reachability mapping process of the  $i$ -th layer. The output image set of the DWM is computed by sequentially applying the reachability mapping  $R_{L_i}$  associated with each layer:

$$\mathcal{I}_{\text{img}} = (R_{L_n} \circ \dots \circ R_{L_1})(S_0). \quad (10)$$

The abstract mapping  $R_{L_i}$  ensures soundness through two mechanisms: (i) for affine layers (e.g., fully connected, convolutional),  $R_{L_i}$  performs an exact mapping of the Star set; (ii) for nonlinear activation layers (e.g., ReLU, sigmoid),  $R_{L_i}$  applies a sound over-approximation provided by StarV. Consequently, the final output set  $\mathcal{I}_{\text{img}}$  is an *ImageStar* [28]. This set captures the *complete envelope of admissible images* that the DWM generates from the initial state set  $S_0$ .

*From ImageStar to Controller and Dynamics.* To close the verification loop, the ImageStar set  $\mathcal{I}_{\text{img}}$  serves as the input to the image-based controller  $C$ . Similar to the DWM, the controller is composed of  $m$  layers,  $C = M_m \circ \dots \circ M_1$ . We compute the reachable set of control actions, denoted as  $U$ , by propagating the image set through the controller's layer-wise abstract operators  $R_{M_j}$ :

$$U = (R_{M_m} \circ \dots \circ R_{M_1})(\mathcal{I}_{\text{img}}). \quad (11)$$

Given the current set of states  $\mathcal{R}_t$  and the action set  $U_t = C(g_\theta(S_t))$  derived from the world-model outputs evaluated in the controller, the closed-loop dynamics update is captured by the abstract system-level transformation  $R_{\text{dyn}}$ . This is implemented using PyBDR [6], a Python-based toolbox for sound reachability analysis of nonlinear dynamical systems, to compute a sound over-approximation of the one-step reachable state set under all admissible state-action pairs.

By iterating over the mapping

$$\mathcal{R}_{t+1} = R_{\text{dyn}}(\mathcal{R}_t, U_t), \quad t = 0, 1, \dots, T-1, \quad (12)$$

we obtain a reachable tube  $\{\mathcal{R}_t\}_{t=0}^T$  over the finite time horizon  $T$ . It can then be checked against the specification (e.g., goal  $G$ ) to produce a verification verdict.



## 5 From World-Model Reachability to Real Guarantees

Surrogate camera models, such as our learned world model, inevitably introduce modeling errors compared to the physical camera system. To transfer the guarantees derived from the surrogate system to the real one, we must first quantify the discrepancy. Without a tractable description of the real system, we opt for a statistical approach. Inspired by our past work on controller approximation [9] and powered by conformal prediction, we bound *trajectory-based discrepancies* between the real and surrogate system. This allows us to find surrogate guarantees that remain valid for the real system.

*Trajectory Dataset.* To quantify the modeling fidelity, we rely on the trajectory dataset  $\mathcal{D}$  collected from the real system, per the problem formulation. It contains trajectories  $\tau_{\text{real}}$  obtained by executing the system with the real camera from initial state  $s_0 \sim D_0$ . For such  $s_0$ , we also obtain a world-model trajectory  $\tau_{\text{wm}}$  by recursively unrolling the DWM, resulting in the following pair:

$$\tau_{\text{real}}(s_0, T) = [s_0, s_1, \dots, s_T], \quad \tau_{\text{wm}}(s_0, T) = [s_0, \hat{s}_1, \dots, \hat{s}_T].$$

*Trajectory Discrepancy as Non-Conformity.* We use the deviations between the real and world-model trajectories as our non-conformity scores. For each pair of trajectories, we define the non-conformity score  $\delta$  as the maximum  $L_1$  distance between the real and world-model states over the entire time horizon  $T$ :

$$\delta = \max_{t=0, \dots, T} \|s_t - \hat{s}_t\|_1.$$

Let  $\{s_0^{(1)}, \dots, s_0^{(k)}\}$  represent independent and identically distributed (i.i.d.) initial states drawn from  $D_0$ , which yields the non-conformity scores  $\{\delta_1, \dots, \delta_k\}$ . Following the standard conformal prediction procedure [26], we append an infinite value to the set, defining  $\delta_{k+1} = \infty$ . It gets selected when the sample size is too small, indicating the absence of a meaningful bound.

*Conformal Prediction Bound.* Conformal prediction provides a statistical upper bound on the trajectory discrepancy for a specified failure probability  $\alpha$ . We sort the non-conformity scores in ascending order and select the  $(1 - \alpha)$  quantile:

$$\Delta_{1-\alpha} := \delta_{(r)}, \quad r = \lceil (k+1)(1-\alpha) \rceil.$$

By the main property of conformal prediction, this bound satisfies:

$$\Pr_{s_0 \sim D_0} \left[ \max_{t \in \{0, \dots, T\}} \|s_t - \hat{s}_t\|_1 \leq \Delta_{1-\alpha} \right] \geq 1 - \alpha,$$

where  $D_0$  is the distribution with support over the initial set  $S_0$ .

*Inflating Reachability with Conformal Bound.* The closed-loop verification with the DWM, per Section 4, produces a reachable tube  $\mathcal{R}_1^{\text{WM}}(S_0), \dots, \mathcal{R}_T^{\text{WM}}(S_0)$ . However, these sets do not account for modeling error. To provide a real-system guarantee, we inflate each world-model reachable set by the conformal bound  $\Delta_{1-\alpha}$ . The inflated reachable set at time step  $t$  is defined as the Minkowski sum of the model’s reachable set and conformal error bound:

$$\hat{\mathcal{R}}_t(S_0) = \{s \in \mathbb{R}^n \mid \exists \hat{s} \in \mathcal{R}_t^{\text{WM}}(S_0) \text{ s.t. } \|s - \hat{s}\|_1 \leq \Delta_{1-\alpha}\}.$$

This is implemented in practice by enlarging the coordinate-wise state bounds extracted from the final reachable set  $\mathcal{R}_T^{\text{WM}}(S_0)$ . In particular, after computing the state-wise lower and upper bounds  $\underline{s}_T$  and  $\bar{s}_T$  that over-approximate the set  $\mathcal{R}_T^{\text{WM}}(S_0)$ , we expand them to  $\underline{s}_T - \Delta_{1-\alpha}$  and  $\bar{s}_T + \Delta_{1-\alpha}$ . Only the final-step bounds are inflated, leaving all intermediate reachable sets unchanged. With this adjustment, the resulting inflated terminal reachable set serves as a statistically rigorous envelope that captures the worst-case discrepancy between the DWM and real trajectories.

*Containment Guarantee.* Inflating our world model with the conformal inflation yields a realistic safety guarantee: with probability at least  $1 - \alpha$ , the inflated reachable sets contain the real system’s trajectories. This containment ensures that if the inflated set does not intersect with the unsafe set, the physical system produces a successful trajectory with a high chance.

**Theorem 1 (Confident Reachable Tube Containment).** *Let  $s_0, \dots, s_T$  be a random trajectory of the real vision-based system over the time horizon  $T$  starting from initial state  $s_0 \sim D_0$ . This trajectory will be contained in the reachable tube  $\hat{\mathcal{R}}_0(S_0), \dots, \hat{\mathcal{R}}_T(S_0)$  constructed by world-model reachability over the support  $S_0$  of distribution  $D_0$  and  $\alpha$ -inflated with conformal prediction over dataset  $\mathcal{D}$ , collected from the same initial distribution  $D_0$ , with probability  $1 - \alpha$ :*

$$\Pr_{s_0 \sim D_0} \left[ \forall t \in \{0, \dots, T\}, \quad s_t \in \hat{\mathcal{R}}_t(S_0) \right] \geq 1 - \alpha.$$

The proof is provided in the Appendix.

**Corollary 1 (Confident Real-System Reachability).** *If Theorem 1 holds and the inflated reachable set  $\hat{\mathcal{R}}_T$  is contained within the goal set  $G$ , the real system state  $s_T$  is guaranteed reach  $G$  with a probability of at least  $1 - \alpha$ :*

$$\hat{\mathcal{R}}_T \subseteq G \implies \mathbb{P}_{s_0 \sim D_0} [s_T \in G] \geq 1 - \alpha.$$

## 6 Experimental Setup

This section introduces the details of the benchmark systems, controller and world model architectures, and the safety specifications for each verification task. We also introduce the baselines used for comparison and highlight how their latent variables affect verification scalability.

### 6.1 Benchmarks and System Architectures

We evaluate our approach on three standard benchmarks commonly used in vision-based verification: *CartPole*, *MountainCar*, and *Pendulum*. Each benchmark consists of a dynamical system, a world model that generates a  $96 \times 96$  grayscale image from a state, and an image-based controller trained with reinforcement learning to map the rendered image to a control action.

*World Model Training.* Our state-based world model is a convolutional decoder that maps each state  $s_t$  to a synthesized image  $\hat{I}_t = g_\theta(s_t)$ . Its architecture contains three fully connected layers followed by two transposed convolution layers with ReLU activations and final pixel clamping to  $[0, 1]$  (full details are in the appendix). For each benchmark, we collect 10,000  $(s, I)$  training pairs by uniformly sampling states over the state space and recording the corresponding camera images. The model is trained with a weighted reconstruction loss and the controller difference loss introduced earlier, using  $\lambda = 10^{-3}$ .

*Image-Based Control Policy.* Each benchmark provides a fixed CNN controller with two convolutional layers and two fully connected layers. Given an input image  $I_t$ , either a real camera frame or a synthesized world-model image, the controller outputs the control input  $u_t = C(I_t)$ . Since controller design is not the focus of this paper, full architecture details are deferred to the appendix.

### 6.2 Reach Specifications, Initial Set Partitioning, and Baseline

The objective is to verify reachability to the goal set  $G$  at time  $T = 20$ , defined as:  $|\theta| \leq 12^\circ$  for *CartPole*,  $x \geq 0.5$  for *MountainCar*, and  $\theta \in [-0.15, 0.15]$  for *Pendulum*. For efficient parallel verification, we divide each initial set  $S_0$  into uniform grid cells. The dimensional ranges and interval are as follows:

- *CartPole*:  $(x_0, \theta_0)$  grid with  $\Delta x = 0.01$ ,  $\Delta \theta = 0.001$ . The position is  $[0.0, 0.6]$  and the angle is  $[0.06, 0.12]$ , with 3600 cells.
- *MountainCar*:  $(x_0, v_0)$  grid with  $\Delta x = 0.01$ ,  $\Delta v = 0.001$ . The position is  $[-0.2, 0.6]$  and the velocity is  $[0.00, 0.08]$ , with 6400 cells.
- *Pendulum*:  $(\theta_0, \omega_0)$  grid with  $\Delta \theta = 0.01$ ,  $\Delta \omega = 0.01$ . The angle is  $[1.0, 2.0]$  and the angular velocity is  $[4.5, 5.0]$ , with 5000 cells.

*Reachability Ground-Truth.* To closely approximate the “ground truth” for reachability, we densely sample 100 initial states from each cell and run the true closed-loop system using real camera images. A cell is labeled successful if and only if *all* the sampled trajectories reach the goal. These success labels are used to compute precision, recall, and F1 scores for our approach.

*Baseline for Comparison.* We compare our method with conditional GAN baselines following prior work [3]. In these models, the generator takes the concatenation of the state  $s_t$  and a latent vector  $z \sim \mathcal{N}(0, I)$  and outputs an image

$\tilde{I}_t = G(s_t, z)$ . During verification, both  $s$  and  $z$  must be bounded. Because  $z$  has no physical meaning, the interval is set to be  $[-0.8, 0.8]$ , the same interval as in the original paper. This latent dimension significantly enlarges the reachable image set because it introduces high-dimensional variability that does not correspond to any physical state, making verification substantially more conservative.

## 7 Results Analysis

This section evaluates the verification with the proposed world model compared to the baseline cGAN. First, we analyze the impact of latent variables on image reconstruction and the resulting pixel-level uncertainty. Next, we present closed-loop verification results using the StarV. Finally, we conduct an ablation study to assess the impact of the controller difference loss on the model’s performance.

### 7.1 Generated Image Bounds Suffer from Latents

Our key insight is that latent variables introduce excessive stochasticity for image generation, which harms the precision needed for formal verification. Although commonly used to ease training and improve image diversity, latent variables produce excessively wide bounds during the reachability analysis.

To quantify the impact of latent variables, we compare the image sets generated by our DWM against the baseline cGAN [15] with the same initial set  $S_0$ . The cGAN incorporates a latent variable  $z$  sampled from a truncated normal distribution:

$$\mathcal{I}_{\text{cGAN}} = \{ G(s, z) \mid s \in S_0, z \sim \mathcal{N}(0, I) \}.$$

In contrast, the image set generated by our DWM depends solely on the state input, defined formally as:

$$\mathcal{I}_{\text{WM}} = \{ g_\theta(s) \mid s \in S_0 \}.$$

Visual comparisons show that the baseline model produces significantly larger pixel-level intervals than our approach, as shown in Figure 2. Specifically, the cGAN generates the pendulum with *high spatial uncertainty*, where it occupies the pixel space that should belong to the background. Furthermore, uncontrolled latent variables introduce *substantial noise* into the background regions. The spatial expansion of the object and background noise inflates the volume of the generated image set, which degrades the controller’s performance downstream.

Moreover, this unnecessary expansion in  $\mathcal{I}_{\text{cGAN}}$  causes approximation errors to accumulate rapidly within the closed-loop reachability. The reachable sets explode when these widened intervals  $\mathcal{I}_{\text{cGAN}}$  propagate through the controller and dynamics over multiple steps. Therefore, the verification process produces excessive false negatives, incorrectly labeling safe initial sets as unsafe because the conservative reachable sets intersect with unsafe regions. This issue makes stochastic latent-variable models poorly suited for high-precision formal verification.

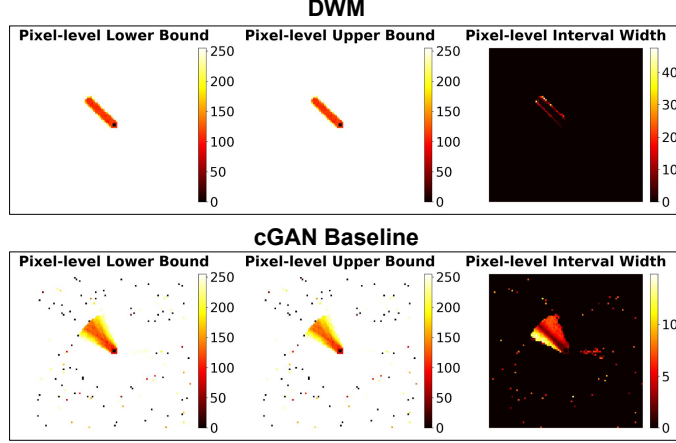


**Fig. 2.** Pixel-level interval comparison under identical physical state for the pendulum benchmark. Both models use the same angle and angular velocity interval  $s = [0.81, 0.82] \times [0.040, 0.041]$ . The cGAN additionally introduces latent variables  $z \in [-0.1, 0.1]^2$ , which injects extra perturbations into the generated images.

## 7.2 Accurate Verification with Deterministic World Models

*Performance Overview.* Our DWM consistently outperforms the baseline across all three benchmarks (Cartpole, MountainCar, and Pendulum). Our proposed method achieves the *highest F1-scores* among three benchmarks (0.9202, 0.9817, and 0.9629, respectively), indicating the best balance between identifying unsafe states and avoiding false alarms, as shown in Table 1. Moreover, the verification times of DWM were 3.5 hours for Pendulum, 1.5 hours for MountainCar, and 2.3 hours for CartPole using 64 CPUs cores on an AMD EPYC 9655P (96-core, Zen 4) compute node in parallel.

**Table 1.** Quantitative comparison of closed-loop verification across Cartpole, MountainCar, and Pendulum benchmarks.

Metric	Cartpole		MountainCar		Pendulum	
	DWM	cGAN [3]	DWM	cGAN [3]	DWM	cGAN [3]
True Negative Rate	1.0000	1.0000	1.0000	0.0000	1.0000	1.0000
Precision	1.0000	1.0000	1.0000	0.6653	1.0000	1.0000
Recall	<b>0.8523</b>	0.7642	0.9641	<b>1.0000</b>	<b>0.9285</b>	0.7618
F1-score	<b>0.9202</b>	0.8663	<b>0.9817</b>	0.7990	<b>0.9629</b>	0.8648

*Analysis of Conservatism.* The excessive baseline conservatism is most evident in the MountainCar case study. While the cGAN achieves a perfect Recall, it

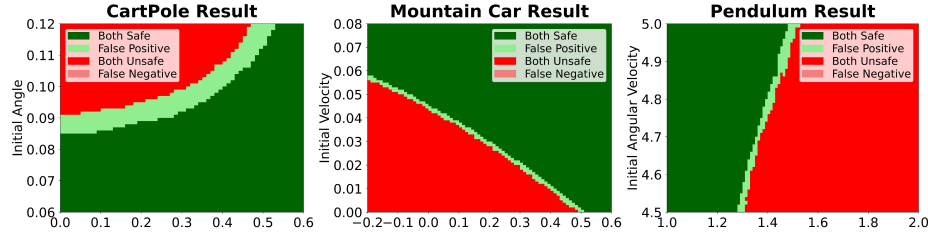


**Fig. 3.** DWM Closed-loop verification with camera roll-out ground-truth across three benchmarks. Dark Green and Red indicate correct classification, while *Light Green* represents conservatism (False Positives: safe cell incorrectly labeled as unsafe).

yields a True Negative Rate (TNR) of 0.0. This indicates that the model is unable to recognize any successful regions: the verifier labels every initial cell as unsuccessful. This occurs because the cGAN’s reachable sets expand to cover the entire state space. In contrast, our method gives a perfect TNR of 1.0, showing tight reachable sets that distinguish between successful and unsuccessful regions.

*Precision and Recall.* Our approach maintains a precision of 1.0 across all benchmarks. This indicates zero false positives: when our verifier labels an initial cell as unsafe, the ground truth is unsafe. Moreover, we achieve this high precision without sacrificing sensitivity. In the Cartpole and Pendulum case studies, our approach demonstrates higher recall rates than the baseline, resulting in a less conservative verification.

### 7.3 High Fidelity of Deterministic World Models

Finally, we quantify the trajectory-level fidelity of different world models using conformal prediction. By sampling  $k$  initial points and propagating them through both the dynamics and the respective world models, we compute the 95% conformal prediction bounds, denoted as  $\Delta_{0.95}$ . A smaller  $\Delta_{0.95}$  indicates that the generated trajectories are more tightly clustered around the ground truth, reflecting superior approximation.

**Table 2.** Trajectory-based conformal prediction bounds ( $\Delta_{0.95}$ ) across world models.

Method	CartPole	MountainCar	Pendulum
cGAN baseline	1.472	0.054	0.358
DWM (no $\mathcal{L}_{\text{ctrl}}$ Loss)	0.111	0.029	0.054
DWM (with $\mathcal{L}_{\text{ctrl}}$ Loss)	<b>0.093</b>	<b>0.022</b>	<b>0.049</b>

Table 2 presents the computed bounds for both baseline and our DWM. The cGAN baseline exhibits large prediction intervals (e.g., 1.472 for CartPole),

caused by the high variance in its latent variable. In contrast, DWM achieves a significant reduction in these bounds across all benchmarks. Furthermore, the ablation study highlights the contribution of the controller difference loss. Incorporating this  $\mathcal{L}_{\text{ctrl}}$  loss yields the tightest bounds for CartPole, MountainCar, and Pendulum (0.093, 0.022, and 0.049 for each). This reduction translates into tighter reachable sets and minimizing false negatives.

**Table 3.** Real-system guarantee transfer with conformal prediction.

Metric	Cartpole		MountainCar		Pendulum	
	Non-CP	CP	Non-CP	CP	Non-CP	CP
True Negative Rate	1.0000	1.0000	1.0000	1.0000	1.0000	1.0000
Precision	1.0000	1.0000	1.0000	1.0000	1.0000	1.0000
Recall	0.8523	0.1304	0.9641	0.9408	0.9285	0.6458
F1-score	0.9202	0.2308	0.9817	0.9695	0.9629	0.7874

Table 3 presents the verification results with and without inflation with the CP bounds. The non-CP results demonstrate that, when evaluated without any robustness guarantees, our method achieves high apparent performance across all benchmarks, with F1 scores above 0.95 and perfect precision. The addition of the CP bound serves as a mathematically grounded layer of guarantee, effectively a “cherry on top” that bridges the model-to-real gap. For dynamics with low error sensitivity, such as MountainCar and Pendulum, adding this guarantee costs little in terms of performance: recall remains high. However, in dynamics with high error amplification, such as Cartpole, the worst-case error bounds significantly inflate the reachable sets, causing a large drop in the recall rate. Crucially, this drop does not indicate a failure of the world model, but the *price of rigor*: CartPole exhibits high sensitivity to modeling error, where even minimal deviations in state or dynamics can rapidly compound into unsafe trajectories.

## 8 Conclusion

In this work, we presented a novel approach for the reachability verification of closed-loop vision-based systems, addressing the challenges of high-dimensional scalability. By training a Deterministic World Model (DWM) with dual loss, we effectively mitigated the compounding overapproximation buildup inherent in prior cGAN-based baselines, thus enabling precise layer-wise reachability analysis via StarV. Our integration of conformal prediction further bridges the model-to-reality gap, transferring the verification results into statistically rigorous safety guarantees for real vision-based systems. Extensive experiments on three benchmarks demonstrate that our approach yields significantly tighter bounds and superior verification accuracy compared to baselines. While the application of conformal bounds introduces necessary conservatism, particularly in unstable dynamics, it reflects the requisite price of rigorous guarantees.

## References

1. Balasubramanian, V., Ho, S.S., Vovk, V.: Conformal prediction for reliable machine learning: theory, adaptations and applications. Newnes (2014)
2. Barber, R.F., Candes, E.J., Ramdas, A., Tibshirani, R.J.: Conformal prediction beyond exchangeability. *The Annals of Statistics* **51**(2), 816–845 (2023)
3. Cai, F., Fan, C., Bak, S.: Scalable surrogate verification of image-based neural network control systems using composition and unrolling. In: *Proceedings of the AAAI Conference on Artificial Intelligence*. vol. 39, pp. 21–30 (2025)
4. Chrysos, G.G., Kossaifi, J., Zafeiriou, S.: Robust conditional generative adversarial networks. *arXiv preprint arXiv:1805.08657* (2018)
5. Dangskul, W., Phattaravatin, K., Rattanaporn, K., Kidjaidure, Y.: Real-time control using convolution neural network for self-driving cars. In: *2021 7th International Conference on Engineering, Applied Sciences and Technology (ICEAST)*. pp. 125–128. IEEE (2021)
6. Ding, J., Wu, T., Liang, Z., Xue, B.: Pybdr: Set-boundary based reachability analysis toolkit in python. In: *International Symposium on Formal Methods*. pp. 140–157. Springer (2024)
7. Everett, M.: Neural network verification in control. In: *2021 60th IEEE Conference on Decision and Control (CDC)*. pp. 6326–6340 (2021). <https://doi.org/10.1109/CDC45484.2021.9683154>
8. Fontana, M., Zeni, G., Vantini, S.: Conformal prediction: a unified review of theory and new challenges. *Bernoulli* **29**(1), 1–23 (2023)
9. Geng, Y., Baldauf, J.B., Dutta, S., Huang, C., Ruchkin, I.: Bridging dimensions: Confident reachability for high-dimensional controllers. In: *International Symposium on Formal Methods*. pp. 381–402. Springer (2024)
10. Guo, J., Nguyen, H.T., Liu, C., Cheah, C.C.: Convolutional neural network-based robot control for an eye-in-hand camera. *IEEE Transactions on Systems, Man, and Cybernetics: Systems* **53**(8), 4764–4775 (2023)
11. Habeeb, P., Deka, N., D’Souza, D., Lodaya, K., Prabhakar, P.: Verification of camera-based autonomous systems. *IEEE Transactions on Computer-Aided Design of Integrated Circuits and Systems* **42**(10), 3450–3463 (2023)
12. Huang, C., Fan, J., Li, W., Chen, X., Zhu, Q.: Reachnn: Reachability analysis of neural-network controlled systems. *ACM Transactions on Embedded Computing Systems (TECS)* **18**(5s), 1–22 (2019)
13. Isola, P., Zhu, J.Y., Zhou, T., Efros, A.A.: Image-to-image translation with conditional adversarial networks. In: *Proceedings of the IEEE conference on computer vision and pattern recognition*. pp. 1125–1134 (2017)
14. Ivanov, R., Weimer, J., Alur, R., Pappas, G.J., Lee, I.: Verisig: verifying safety properties of hybrid systems with neural network controllers. In: *Proceedings of the 22nd ACM International Conference on Hybrid Systems: Computation and Control*. pp. 169–178 (2019)
15. Katz, S.M., Corso, A.L., Strong, C.A., Kochenderfer, M.J.: Verification of image-based neural network controllers using generative models. *Journal of Aerospace Information Systems* **19**(9), 574–584 (2022)
16. Kochdumper, N., Schilling, C., Althoff, M., Bak, S.: Open-and closed-loop neural network verification using polynomial zonotopes. In: *NASA Formal Methods Symposium*. pp. 16–36. Springer (2023)
17. Liu, C., Arnon, T., Lazarus, C., Strong, C., Barrett, C., Kochenderfer, M.J., et al.: Algorithms for verifying deep neural networks. *Foundations and Trends® in Optimization* **4**(3-4), 244–404 (2021)



18. Lopez, D.M., Musau, P., Tran, H.D., Johnson, T.T.: Verification of closed-loop systems with neural network controllers. In: ARCH@ CPSIoTWeek. pp. 201–210 (2019)
19. Mersch, B., Höllen, T., Zhao, K., Stachniss, C., Roscher, R.: Maneuver-based trajectory prediction for self-driving cars using spatio-temporal convolutional networks. In: 2021 IEEE/RSJ International Conference on Intelligent Robots and Systems (IROS). pp. 4888–4895. IEEE (2021)
20. Mitra, S., Păsăreanu, C., Prabhakar, P., Seshia, S.A., Mangal, R., Li, Y., Watson, C., Gopinath, D., Yu, H.: Formal verification techniques for vision-based autonomous systems—a survey. In: Principles of Verification: Cycling the Probabilistic Landscape: Essays Dedicated to Joost-Pieter Katoen on the Occasion of His 60th Birthday, Part III, pp. 89–108. Springer (2024)
21. Mitra, S., Păsăreanu, C., Prabhakar, P., Seshia, S.A., Mangal, R., Li, Y., Watson, C., Gopinath, D., Yu, H.: Formal verification techniques for vision-based autonomous systems—a survey. In: Principles of Verification: Cycling the Probabilistic Landscape: Essays Dedicated to Joost-Pieter Katoen on the Occasion of His 60th Birthday, Part III, pp. 89–108. Springer (2024)
22. Ostrovsky, M., Barrett, C., Katz, G.: An abstraction-refinement approach to verifying convolutional neural networks. In: International Symposium on Automated Technology for Verification and Analysis. pp. 391–396. Springer (2022)
23. Rodziewicz-Bielewicz, J., Korzena, M.: Sparse convolutional neural network for localization and orientation prediction and application to drone control (2024)
24. Rossi, F., Bernardeschi, C., Cococcioni, M.: Neural networks in closed-loop systems: Verification using interval arithmetic and formal prover. *Engineering Applications of Artificial Intelligence* **137**, 109238 (2024)
25. Santa Cruz, U., Shoukry, Y.: Nnlander-verif: A neural network formal verification framework for vision-based autonomous aircraft landing. In: NASA Formal Methods Symposium. pp. 213–230. Springer (2022)
26. Shafer, G., Vovk, V.: A tutorial on conformal prediction. *Journal of Machine Learning Research* **9**(3) (2008)
27. Sobolewski, C., Mao, Z., Vejre, K., Ruchkin, I.: Generalizable image repair for robust visual autonomous racing. arXiv preprint arXiv:2503.05911 (2025)
28. Tran, H.D., Bak, S., Xiang, W., Johnson, T.T.: Verification of deep convolutional neural networks using imagestars. In: International conference on computer aided verification. pp. 18–42. Springer (2020)
29. Tran, H.D., Choi, S.W., Li, Y., Liu, Q., Okamoto, H., Hoxha, B., Fainekos, G.: Starv: A qualitative and quantitative verification tool for learning-enabled systems. In: International Conference on Computer Aided Verification. pp. 376–394. Springer (2025)
30. Tran, H.D., Choi, S.W., Yang, X., Yamaguchi, T., Hoxha, B., Prokhorov, D.: Verification of recurrent neural networks with star reachability. In: Proceedings of the 26th ACM International Conference on Hybrid Systems: Computation and Control. pp. 1–13 (2023)
31. Tran, H.D., Manzananas Lopez, D., Musau, P., Yang, X., Nguyen, L.V., Xiang, W., Johnson, T.T.: Star-based reachability analysis of deep neural networks. In: International symposium on formal methods. pp. 670–686. Springer (2019)
32. Tran, H.D., Pal, N., Musau, P., Lopez, D.M., Hamilton, N., Yang, X., Bak, S., Johnson, T.T.: Robustness verification of semantic segmentation neural networks using relaxed reachability. In: International conference on computer aided verification. pp. 263–286. Springer (2021)

33. Usman, M., Noller, Y., Păsăreanu, C.S., Sun, Y., Gopinath, D.: Neurospf: A tool for the symbolic analysis of neural networks. In: 2021 IEEE/ACM 43rd International Conference on Software Engineering: Companion Proceedings (ICSE-Companion). pp. 25–28. IEEE (2021)
34. Waite, T., Geng, Y., Turnquist, T., Ruchkin, I., Ivanov, R.: State-Dependent Conformal Perception Bounds for Neuro-Symbolic Verification of Autonomous Systems. In: Proc. of 2nd International Conference on Neuro-symbolic Systems (NeuS). PMLR, Philadelphia, PA, USA (Feb 2025). <https://doi.org/10.48550/arXiv.2502.21308>
35. Wang, Y., Zhou, W., Fan, J., Wang, Z., Li, J., Chen, X., Huang, C., Li, W., Zhu, Q.: Polar-express: Efficient and precise formal reachability analysis of neural-network controlled systems. *IEEE Transactions on Computer-Aided Design of Integrated Circuits and Systems* **43**(3), 994–1007 (2023)
36. Yang, Y., Malaviya, C., Fernandez, J., Swayamdipta, S., Le Bras, R., Wang, J.P., Bhagavatula, C., Choi, Y., Downey, D.: Generative data augmentation for commonsense reasoning. In: Findings of the Association for Computational Linguistics: EMNLP 2020. pp. 1008–1025 (2020)
37. Zheng, C., Wu, G., Li, C.: Toward understanding generative data augmentation. *Advances in neural information processing systems* **36**, 54046–54060 (2023)
38. Zheng, H., Rajadnya, S., Zakhor, A.: Monocular depth estimation for drone obstacle avoidance in indoor environments. In: 2024 IEEE/RSJ International Conference on Intelligent Robots and Systems (IROS). pp. 10027–10034 (2024). <https://doi.org/10.1109/IROS58592.2024.10802577>
39. Zhu, J.Y., Zhang, R., Pathak, D., Darrell, T., Efros, A.A., Wang, O., Shechtman, E.: Toward multimodal image-to-image translation. *Advances in neural information processing systems* **30** (2017)

## 9 Appendix

This appendix provides the theorem proof, the details of neural architectures for control and world modeling, and a detailed description of the verification procedure.

### 9.1 Proof

*Proof.* Let  $\mathcal{D} = \{\tau^{(i)}\}_{i=1}^N$  be the calibration dataset consisting of  $N$  trajectories collected from the real system, where the initial state of each trajectory  $\{(s_0^{(1)}, \dots, s_0^{(N)})\}$  is generated i.i.d. from the initial-state distribution  $D_0$ .

We define the non-conformity score  $\delta_i$  for the  $i$ -th calibration trajectory as the maximum  $L_1$ -deviation between the ground truth state  $s_t^{(i)}$  and the corresponding deterministic world model prediction  $\hat{s}_t^{(i)}$  over the horizon  $T$ :

$$\delta_i = \max_{t \in \{0, \dots, T\}} \|s_t^{(i)} - \hat{s}_t^{(i)}\|_1.$$

According to the methodology of conformal prediction, given a user-specified error rate  $\alpha \in (0, 1)$ , we compute the quantile  $\Delta_{1-\alpha}$  such that, for a new test trajectory  $\tau^{\text{new}}$  drawn independently from the same distribution (thus satisfying exchangeability), the non-conformity score satisfies the following:

$$\Pr_{s_0 \sim D_0} \left[ \max_{t \in \{0, \dots, T\}} \|s_t - \hat{s}_t\|_1 \leq \Delta_{1-\alpha} \right] \geq 1 - \alpha.$$

This inequality implies that with probability at least  $1 - \alpha$ , the real state  $s_t$  at any time step  $t$  lies within the  $L_1$ -ball of radius  $\Delta_{1-\alpha}$  centered at the world model prediction  $\hat{s}_t$ :

$$\forall t, \quad \|s_t - \hat{s}_t\|_1 \leq \Delta_{1-\alpha}.$$

Based on the world-model reachability analysis, the nominal model predicted state  $\hat{s}_t$  is contained within the world model reachable set; i.e.,  $\hat{s}_t \in \mathcal{R}_t^{\text{WM}}(S_0)$ . Combining this with the conformal bound, we have:

$$s_t \in \{s \mid \exists \hat{s} \in \mathcal{R}_t^{\text{WM}}(S_0) \text{ s.t. } \|s - \hat{s}\|_1 \leq \Delta_{1-\alpha}\}.$$

This set is exactly the definition of the inflated reachable set  $\hat{\mathcal{R}}_t(S_0)$ . Therefore, the event defined in the previous equation implies the real state  $s_t \in \hat{\mathcal{R}}_t(S_0)$  for all  $t \in \{0, \dots, T\}$ . Consequently:

$$\Pr_{s_0 \sim D_0} \left[ \forall t \in \{0, \dots, T\}, \quad s_t \in \hat{\mathcal{R}}_t(S_0) \right] \geq 1 - \alpha.$$

### 9.2 World Model and Controller Architectures

For all three benchmarks, the world model is implemented as a state-based decoder  $g_\theta : \mathbb{R}^2 \rightarrow \mathbb{R}^{1 \times 96 \times 96}$  that maps a 2-dimensional state to a  $96 \times 96$  grayscale

image. The image-based controller  $C$  maps the rendered image to a scalar action. The decoder architecture is identical across CartPole, MountainCar, and Pendulum; the controllers share the same convolutional backbone and differ only in the final activation (Sigmoid for CartPole, Tanh for MountainCar and Pendulum).

**Table 4.** World model decoder architecture (all benchmarks).

<b>Decoder <math>g_\theta</math> (state <math>\rightarrow</math> image)</b>
Input state $s \in \mathbb{R}^2$
Dense $\rightarrow 32$ , ReLU
Dense $\rightarrow 64$ , ReLU
Dense $\rightarrow 3 \cdot 12 \cdot 12$ , ReLU
Reshape $\rightarrow 3 \times 12 \times 12$
ConvTranspose 3 $\rightarrow 4$ , kernel $4 \times 4$ , stride 2, padding 1, ReLU
ConvTranspose 4 $\rightarrow 8$ , kernel $4 \times 4$ , stride 2, padding 1, ReLU
ConvTranspose 8 $\rightarrow 1$ , kernel $4 \times 4$ , stride 2, padding 1, SatLin

**Table 5.** Image-based controller architectures.

<b>CartPole controller <math>C_{CP}</math> (image <math>\rightarrow</math> action)</b>
Input image $\tilde{I} \in \mathbb{R}^{1 \times 96 \times 96}$ (grayscale)
Conv 1 $\rightarrow 4$ , kernel $4 \times 4$ , stride 2, padding 1, ReLU
Conv 4 $\rightarrow 1$ , kernel $4 \times 4$ , stride 2, padding 1, ReLU
Flatten $\rightarrow 24 \times 24$
Dense $\rightarrow 64$ , ReLU
Dense $\rightarrow 1$ , Sigmoid
<b>MountainCar / Pendulum controller <math>C_{MC}, C_{Pen}</math> (image <math>\rightarrow</math> action)</b>
Input image $\tilde{I} \in \mathbb{R}^{1 \times 96 \times 96}$ (grayscale)
Conv 1 $\rightarrow 4$ , kernel $4 \times 4$ , stride 2, padding 1, ReLU
Conv 4 $\rightarrow 1$ , kernel $4 \times 4$ , stride 2, padding 1, ReLU
Flatten $\rightarrow 24 \times 24$
Dense $\rightarrow 64$ , ReLU
Dense $\rightarrow 1$ , Tanh

### 9.3 Closed-Loop Verification Procedure

*Formal Description.* At time  $t$ , the uncertainty over the physical state is represented as a Star set  $S_t \subseteq \mathbb{R}^d$  of the form

$$S_t = \{s \in \mathbb{R}^d \mid s = c_t + V_t \alpha, C_t \alpha \leq d_t, \ell_t \leq \alpha \leq u_t\},$$

where  $c_t \in \mathbb{R}^d$  is the center,  $V_t \in \mathbb{R}^{d \times p}$  the basis matrix, and  $\alpha \in \mathbb{R}^p$  are predicate variables constrained by the linear predicate set

$$\mathcal{A}_t = \{\alpha \mid C_t \alpha \leq d_t, \ell_t \leq \alpha \leq u_t\}. \quad (13)$$

For each state component  $i$ , its exact range is obtained by solving two linear programs:

$$\underline{s}_i^t = \min_{\alpha \in \mathcal{A}_t} (c_{t,i} + V_{t,i}\alpha), \quad \bar{s}_i^t = \max_{\alpha \in \mathcal{A}_t} (c_{t,i} + V_{t,i}\alpha), \quad (14)$$

so that each dimension admits an interval  $[\underline{s}_i^t, \bar{s}_i^t]$  consistent with the Star constraints. In our closed-loop experiments we consider a two-dimensional state ( $d = 2$ ), so  $s_t = (s_t^{(1)}, s_t^{(2)})^\top$  and the vectors  $\underline{s}^t, \bar{s}^t \in \mathbb{R}^2$  collect the bounds  $\underline{s}_i^t, \bar{s}_i^t$  for  $i = 1, 2$ .

The trained world model  $g_\theta$  is decomposed into  $n$  layers  $g_\theta = L_n \circ \dots \circ L_1$ , and each layer is associated with a Star-based abstract transformer  $R_{L_i}$ . Given  $S_t$ , the reachable set of synthesized images is the ImageStar

$$\mathcal{I}_t = R_{g_\theta}(S_t) := (R_{L_n} \circ \dots \circ R_{L_1})(S_t), \quad (15)$$

where affine layers (fully connected and transposed convolutions) are propagated exactly and nonlinear layers (ReLU and pixel-saturation) are handled using StarV's sound over-approximation transformers.

The image-based controller  $C$  is likewise written as  $C = M_m \circ \dots \circ M_1$  with abstract transformers  $R_{M_j}$ . Propagating  $\mathcal{I}_t$  through  $C$  yields the reachable action set

$$A_t = R_C(\mathcal{I}_t) := (R_{M_m} \circ \dots \circ R_{M_1})(\mathcal{I}_t), \quad (16)$$

represented as a one-dimensional Star set over the control input. The corresponding scalar control bounds are obtained by optimizing over the action Star:

$$u_{\min}^t = \min_{u \in A_t} u, \quad u_{\max}^t = \max_{u \in A_t} u. \quad (17)$$

The plant dynamics are handled by PyBDR, which implements a system-level transformer  $R_{\text{dyn}}$  that over-approximates one-step reachable states from bounded state and action intervals. Given the state bounds  $\underline{s}^t, \bar{s}^t \in \mathbb{R}^2$  obtained from  $S_t$  as above and the action bounds  $u_{\min}^t, u_{\max}^t$ , PyBDR returns new state bounds

$$[\underline{s}^{t+1}, \bar{s}^{t+1}] = R_{\text{dyn}}(\underline{s}^t, \bar{s}^t, u_{\min}^t, u_{\max}^t), \quad (18)$$

where the bounds are understood element-wise in  $\mathbb{R}^2$ . We then wrap these bounds back into a Star set

$$S_{t+1} = \text{Star}(\underline{s}^{t+1}, \bar{s}^{t+1}), \quad (19)$$

which serves as the input set for the next time step. Iterating this procedure for  $t = 0, \dots, T-1$  yields a sequence of closed-loop reachable sets  $\{S_t\}_{t=0}^T$  that can be checked against the safety specification  $\mathcal{X}_{\text{safe}}$  by testing whether  $S_t \cap \mathcal{X}_{\text{unsafe}} = \emptyset$  for all  $t$ .

*Closed-Loop One-Step Operator.* Combining the components above, we define a closed-loop one-step operator  $\Phi : \mathcal{S} \rightarrow \mathcal{S}$  on the space of state Star sets. Given

a state set  $S_t$ , the world model, controller, and dynamics transformers produce the next state set  $S_{t+1}$  by

$$S_{t+1} = \Phi(S_t) := \text{Star}\left(R_{\text{dyn}}(\underline{s}^t, \bar{s}^t, u_{\min}^t, u_{\max}^t)\right), \quad (20)$$

where  $\underline{s}^t, \bar{s}^t$  are obtained from  $S_t$  via the linear programs above, and  $u_{\min}^t, u_{\max}^t$  are obtained from  $A_t = R_C(R_{g_\theta}(S_t))$  via the scalar optimizations over the action Star. The outer  $\text{Star}(\cdot)$  wraps the resulting two-dimensional state bounds into a hyper-rectangular Star set.

*Multi-Step Closed-Loop Reachability.* For a fixed initial state set  $S_0$ , the  $T$ -step closed-loop reachable sets are obtained by iterating the operator  $\Phi$ :

$$S_t = \Phi^t(S_0), \quad t = 0, 1, \dots, T, \quad (21)$$

where  $\Phi^0$  is the identity map and  $\Phi^{t+1} = \Phi \circ \Phi^t$  for  $t \geq 0$ . In our experiments, we typically take  $T = 20$  and record the entire sequence  $\{S_t\}_{t=0}^T$ , together with the associated two-dimensional state bounds  $\underline{s}^t, \bar{s}^t$  computed from each Star set, to visualize the evolution of the closed-loop uncertainty over time.

*Full-Loop Safety Map over Initial Cells.* To construct the safety maps shown in our figures, we discretize the two-dimensional initial state space into a grid of axis-aligned cells. Let  $\{I_j^{(1)}\}_{j=1}^{N_1}$  be a partition of the range of the first state component and  $\{I_i^{(2)}\}_{i=1}^{N_2}$  a partition of the range of the second state component, with  $I_j^{(1)} = [\underline{s}_j^{(1)}, \bar{s}_j^{(1)}]$  and  $I_i^{(2)} = [\underline{s}_i^{(2)}, \bar{s}_i^{(2)}]$ . For each cell  $(i, j)$  we define an initial state set

$$S_0^{(i,j)} = \text{Star}\left([\underline{s}_j^{(1)}, \bar{s}_j^{(1)}] \times [\underline{s}_i^{(2)}, \bar{s}_i^{(2)}]\right), \quad (22)$$

corresponding to bounded initial values of the two state coordinates. We then apply the closed-loop operator (20) for  $T$  steps:

$$S_t^{(i,j)} = \Phi^t(S_0^{(i,j)}), \quad t = 0, 1, \dots, T. \quad (23)$$

Let  $\mathcal{X}_{\text{unsafe}}$  denote the unsafe region in the two-dimensional state space (e.g., all states with either coordinate exceeding a prescribed threshold). Each cell  $(i, j)$  is classified as *safe* if all reachable sets remain disjoint from the unsafe region,

$$\gamma_{i,j} = 1 \iff S_t^{(i,j)} \cap \mathcal{X}_{\text{unsafe}} = \emptyset \text{ for all } t = 0, \dots, T, \quad (24)$$

and as *unsafe* otherwise ( $\gamma_{i,j} = 0$ ). The resulting matrix  $\Gamma = [\gamma_{i,j}] \in \{0, 1\}^{N_2 \times N_1}$  is rendered as the red-green safety map over the initial conditions used in our experiments.